

Final Draft
of the original manuscript:

Zhang, Y.; Blawert, C.; Tang, S.; Hu, J.; Mohedano, M.; Zheludkevich, M.L.;
Kainer, K.U.:

**Influence of surface pre-treatment on the deposition and
corrosion properties of hydrophobic coatings on a
magnesium alloy**

In: Corrosion Science (2016) Elsevier

DOI: [10.1016/j.corsci.2016.08.013](https://doi.org/10.1016/j.corsci.2016.08.013)

Influence of surface pre-treatment on the deposition and corrosion properties of hydrophobic coatings on a magnesium alloy

Yufen Zhang^{a,b}, Carsten Blawert^{b,*}, Shawei Tang^a, Jin Hu^{a,*}, Marta Mohedano^b,

Mikhail L. Zheludkevich^{b,c}, Karl Ulrich Kainer^b

^a School of Materials Science and Engineering, Harbin Institute of Technology, Harbin 150001, P.R. China

^bInstitute of Materials Research, Helmholtz-Zentrum Geesthacht Zentrum für Material- und Küstenforschung GmbH, Max-Planck-Str. 1, Geesthacht 21502, Germany

^cDepartment of Materials and Ceramics Engineering, CICECO, University of Aveiro, 3810-193 Aveiro, Portugal

Abstract

Calcium stearate based hydrophobic coatings were deposited on pre-treated Mg alloy substrates. **The influence of four different pre-treatments including plasma electrolytic oxidation (as prepared and etched), anodizing and hydrothermal treatment was studied.** The results indicate that the pre-treatments have strong influences on the morphology, thickness, and wettability of the coatings, without affecting their phase composition. **The coating system based on the etched plasma electrolytic oxidation pre-treatment shows the best corrosion resistance in a simulated body fluid.** The superior protection effect is mainly related to the differences in the morphologies and thickness of the pre-treatment layers.

Keywords: A. Magnesium; B. EIS; B. Polarization; B. SEM; B. XRD

* Corresponding author. BOX 433, School of Materials Science and Engineering, Harbin Institute of Technology, Harbin 150001, P.R. China.

Tel.: +86 451 86415894; Fax: +86 451 86413921.

E-mail address: hujin@hit.edu.cn (J. Hu)

* Corresponding author. Helmholtz-Zentrum Geesthacht Zentrum für Material- und Küstenforschung GmbH, Institute of Materials Research, Max-Planck-Str. 1, Geesthacht 21502, Germany.

Tel.: +49 4152 87 1991; fax: +49 4152 87 2660.

E-mail address: carsten.blawert@hzg.de (C. Blawert).

1. Introduction

Magnesium based alloys offer many beneficial properties such as low density, high strength and good biocompatibility [1, 2]. Additionally, they are considered as promising candidates for construction of biomedical devices [2-8] and have attracted increasing attention for load-bearing biocompatible implant applications [9-11]. However, the relatively poor corrosion resistance of magnesium alloys in aggressive environments limits their application range.

Applying a protective coating is an effective way to improve the corrosion resistance of magnesium alloys. Several coating approaches have been followed including chemical conversion processes, electro/electroless plating, anodic/micro-arc oxidation, sol-gel and physical vapor deposition [12-21]. However, when talking about biomedical applications some of those coatings are not suitable, because of toxicity or release of unwanted debris [14, 22].

A recent trend to protect magnesium alloys is the development of hydrophobic coatings, which can provide self-cleaning, anti-contamination and anti-icing properties as well as corrosion protection [23-27]. Normally, the hydrophobicity can be achieved by a combination of micro/nanostructuring the surface and low surface energy. High hydrophobicity ensures an important decrease of the contact area of the material surface with the corrosive medium and the fraction of solid at the solid/water interface is normally around 20% [28, 29]. Thus, hydrophobic coatings can offer an additional delay of the corrosion processes especially in the initial stages of contact with electrolyte or in the case of exposure to wet-dry cycles. In addition, good hemocompatibility and low bacteria adhesion were reported for metallic substrates coated with hydrophobic coatings [30, 31], suggesting a good potential for biomedical applications. The improvement of corrosion resistance of magnesium alloys via application of hydrophobic coatings has been reported in previous studies [30-34]. However, most of the studies on hydrophobic coatings have been carried out on copper, aluminum, titanium and other engineering

metallic substrates [35-39]. Traditionally, a two-step process is applied including the development of a micro/nanostructure which is followed by the modification of the surface with a low surface energy material [23, 29, 40, 41]. In the case of magnesium, a rough surface was obtained by hydrothermal treatment [30], micro-arc oxidation [32], in situ crystallization [33], or etching [31, 34]. Subsequently, stearic acid [30-32, 34] or the silane coupling agents [33] are applied in order to reduce the surface energy. Recently, electrodeposition processes, combining the two steps together, have been suggested to prepare hydrophobic coatings in an effective and time saving one-step approach. Such coatings have been produced on copper and zinc, based on zinc-laurylamine, Cu(II)-laurylamine, and zinc tetradecanoate [42-46]. These studies have focused on the self-cleaning effect and the corrosion protection performance of the hydrophobic coatings. Moreover, the effect of processing parameters on the formation of hydrophobic coatings was also investigated. However, the deposition of hydrophobic coatings on magnesium and its alloys with a one-step electrodeposition method is scarcely explored.

Many factors can affect the microstructure and the corrosion resistance of hydrophobic coatings on magnesium alloys [23, 24, 47]. Change in coating composition, deposition time, and other processing parameters can lead to different results. Recently, we have successfully demonstrated electrodeposition of calcium stearate coating on an anodized magnesium alloy. The obtained coatings ensure high hydrophobicity and the formation mechanism of such coatings has been discussed in detail in our previous work [48]. It was found that the deposition parameters have a significant effect on the corrosion properties of such a coating [48]. However, relatively little is known about the effect of pre-treatment on the deposition of the hydrophobic coating on the magnesium alloy. Moreover, the influence of pre-treatment on the effectiveness of the corrosion protection of the magnesium alloy in simulated body fluid is not studied yet. In this work, we focus on understanding the role of pre-treatment on the microstructure and

electrochemical characteristic of the hydrophobic coating on the AZ21 magnesium alloy. The corrosion mechanisms of the pre-treated magnesium alloy with and without the hydrophobic coatings are also discussed in detail.

2. Experimental

2.1 Materials

Commercial magnesium alloy AZ21 sheet (0.6 mm thickness) was cut into rectangular specimen of 20 mm × 40 mm. The chemical composition of the material is shown in Table 1. Prior to the pre-treatment, the specimens were abraded with SiC emery paper up to 1500 grade, cleaned in deionized water and ethanol and dried in compressed air.

2.2 Pre-treatments

Four different pre-treatments were carried out on the magnesium alloy. The details of treatment bath composition and process parameters are shown in Table 2. The first pre-treatment was a plasma electrolytic oxidation (PEO) treatment only. The PEO process was carried out in an alkaline phosphate-based electrolyte (2 g/L Ca(OH)₂ and 12 g/L Na₃PO₄) using a pulsed DC power supply ($t_{on} : t_{off} = 0.5 \text{ ms} : 4.5 \text{ ms}$) under a constant voltage of 380 V for 5 min limiting the current density to a maximum of 0.05 A/cm². During the PEO process, the specimen and a stainless steel tube were used as anode and cathode, respectively. The electrolyte was continuously agitated combining mechanical stirring with continuous air bubbling to ensure the uniform distribution of the particles in the electrolyte and to avoid their sedimentation. The temperature of the PEO electrolyte was kept at 20 °C by a water cooling system. In the second pre-treatment, the PEO coated magnesium alloy was additionally etched in a diluted phosphoric acid (60 g/L H₃PO₄) for 10 s at room temperature.

The third pre-treatment was a conventional anodizing treatment. The anodizing process was carried out with a DC power supply applying 4 V for 10 min. The specimen was used as the

anode and a steel sheet was used as the cathode. The electrolyte contained 2.5 g/L sodium oxalate ($\text{Na}_2\text{C}_2\text{O}_4$), 240 g/L sodium hydroxide (NaOH), 65 ml/L ethanediol ($\text{C}_2\text{H}_6\text{O}_2$) and the solvent was deionized water. During the process, a magnetic stirrer was used and the electrolyte temperature was controlled at 40 °C.

The fourth pre-treatment was a hydrothermal treatment method exposing the specimens to 90 °C and 90% humidity in a climate chamber (Weiss WK111-340).

The corresponding pre-treatments are named PEO (plasma electrolytic oxidation), EPEO (etched plasma electrolytic oxidation), AT (anodizing treatment), and HT (hydrothermal treatment), respectively.

2.3 Deposition of the hydrophobic coatings

The coatings were deposited on the pre-treated magnesium alloy using a two-electrode cell, in which, the pre-treated substrates were used as the cathode and a graphite sheet was used as the anode. The electrolyte contained 0.05 mol/L calcium nitrate ($\text{Ca}(\text{NO}_3)_2$), 0.05 mol/L stearic acid and the solvent was ethanol ($\geq 99.5\%$). The deposition process was performed at 50 V for 60 min using a DC power supply (Elektro-Automatik GmbH, EA-PS 8720-15) in voltage control mode at room temperature. The current density vs. time curve was recorded during the first 900 s of the deposition process. After deposition, the coated specimens were cleaned with ethanol and dried in air. The details of electrolyte composition and parameters of the fabrication process are summarized in Table 3. In order to simplify the nomenclature of the hydrophobic coatings formed on different pre-treated substrates, these coating systems are referred to as PEO-HC, EPEO-HC, AT-HC, and HT-HC, respectively. If not a specific coating is addressed the combination of pre-treatment and hydrophobic coating is referred to as full coating system. It should be noted that no hydrophobic coating can be deposited on the as prepared PEO, thus, we will not report the relevant information of PEO-HC in the result section.

2.4 Characterization

The surface morphologies and cross-sectional morphologies of the pre-treated substrates as well as of the full coating systems were studied using a Tescan Vega3 SB scanning electron microscopy (SEM) equipped with an energy dispersive spectrometer (EDS). Phase composition was **determined** by X-ray diffraction (XRD) with a Bruker X-ray diffractometer using Cu K α radiation at 40 kV and 40 mA. The data collection was performed by $\theta/2\theta$ scan method at a scan speed of 0.01 °/s in the range from 20 ° to 80 °. Static water contact angles were measured with a contact angle meter (Drop Shape Analyzer – DSA100, Krüss, Germany) at ambient temperature. The volume of the water droplets used in the measurements was 3 μ L. In order to get a reliable result, the value of the static contact angle was recorded after the water droplet stayed for 1 min on the coating surface **and the measurements were repeated** three times for each specimen.

2.5 Electrochemical measurements

All the electrochemical tests were performed in a simulated body fluid (SBF) at 37 \pm 0.5 °C using a Gamry AC computer-controlled potentiostat. The SBF contained 8.035 g/L NaCl, 0.355 g/L NaHCO₃, 0.225 g/L KCl, 0.231 g/L K₂HPO₄·3H₂O, 0.311 g/L MgCl₂·6H₂O, 0.292 g/L CaCl₂ and 0.072 g/L Na₂SO₄ [49]. The pH of the SBF was adjusted to 7.4 **using** 1.0 mol/L HCl and tris (hydroxymethyl) aminomethane ((CH₂OH)₃CNH₂). All tests were measured in a three-electrode cell with a saturated calomel reference electrode (SCE) and a platinum counter electrode. The specimen was used as the working electrode with an exposed surface area of 0.5 cm². For recording the potentiodynamic polarization curves, the open circuit potential (OCP) was set to stabilize for 30 min and the scanning rate was set to 0.5 mV/s. Electrochemical impedance spectroscopy (EIS) measurements were performed by applying a sinusoidal potential perturbation of 10 mV RMS (at OCP) and a frequency sweep from 10⁵ Hz to 10⁻² Hz. All electrochemical

tests were repeated three times with a good reproducibility. EIS results were analyzed by fitting data with ZSimpWin software.

3. Results

3.1 Characterization of the pre-treated surfaces

To understand the effect of the surface pre-treatment on the formation and the corrosion resistance of the hydrophobic coating, the surface morphology, chemical composition and microstructure of the pre-treated magnesium alloy were characterized.

Fig. 1 shows the XRD diffraction patterns of different pre-treated substrates. The diffraction peaks of Mg and MgO can be found in all the cases, indicating that MgO is always formed as a result of the pre-treatments. However, the corresponding intensities of MgO for PEO and EPEO are higher compared to the others, suggesting that the PEO and EPEO pre-treated layers are probably thicker.

EDS was used to determine the elemental composition of AZ21 Mg alloy and the pre-treated substrates (Table 4). The appearance of a high phosphorus concentration after PEO or EPEO pre-treatment is interesting, because there is no phosphorus containing phase detected by the XRD measurements. The reason is probably related to a nanocrystalline or amorphous structure of the phosphorus containing phase. The etching of the PEO layer results in an increase of the magnesium concentration from 39.2% (PEO) to 42.6% (EPEO), and the content of phosphorus decreases from 17.7% to 16.0%, respectively. The reason might be that some soluble phosphates in the PEO layer are more easily dissolved while the sample is exposed to the phosphoric acid.

Fig. 2 shows the SEM images of different pre-treated substrates. Fig. 2a reveals a typical morphology of the PEO layer with numerous micro-pores owing to the discharges during the PEO process. Discontinuous micro-cracks are observed as well. Compared to the original PEO layer (Fig. 2a), more pores and a higher amount of micro-cracks appear on the surface of the

EPEO layer (Fig. 2b). The number of open pores increases obviously, indicating that some closed pores are opened during the phosphoric acid etching process. Furthermore, some pores with volcano shape appear on the surface of the layer (insets in Fig. 2b) after the etching process giving additional evidence for material removal. The **AT** surface (Fig. 2c) demonstrates cracks and islands-like rough structure. The surface morphology of the **HT** layer is shown in Fig. 2d. The **HT** layer is very thin and the typical topographical features such as grinding scratches are still visible. A high magnification view reveals interlacing plate-like structures (inset in Fig. 2d). This is a typical appearance of hydroxides on magnesium and magnesium alloy surfaces [47, 50].

3.2 Deposition, morphology and microstructure of the hydrophobic coating

In order to understand the effect of pre-treatment on the formation of the hydrophobic coating, the current density was monitored during the first 900 s of the **cathodic** electrodeposition process, as shown in Fig. 3. All the curves show the same trend, except the sample pre-treated with PEO. During the whole process, the current density of the sample with PEO pre-treatment is near zero **and no hydrogen bubbles escape from the cathode**, indicating that the barrier properties of the PEO layer are too high to deposit a coating. During the electrodeposition process, the voltage applied between the two electrodes drops across this layer, leading to an insufficient gradient of the electrical field appearing in the electrolyte. Therefore almost no coating was deposited on the sample surface. However, a coating can form on the surface of the **EPEO**. The phosphoric acid etching damages the barrier properties of the PEO layer, resulting in a similar current density vs. time response compared to other two pre-treatments. The current densities drop significantly in the first 90 s, implying that the resistance of the **pre-treated** substrates increases evidently with the coating time. In the initial deposition stage, a fast nucleation of the coating at many different sides leads to the formation of a coating on the pre-treated substrates. In the next stage, the current densities decrease faintly, suggesting that the surface coverage of the

coatings is almost complete. Finally, the surfaces of the pre-treated substrates are covered completely by the coating and the current densities remain at a low value, indicating that the coating grows slowly but continuously on the pre-treated substrates. Thus, the hydrophobic coating can form on different pre-treated substrates, as long as the barrier properties of the pre-treatment layers are not too high to drive the deposition process.

The formation mechanism of the hydrophobic coating on different pre-treated substrates can be proposed as follows. $\text{Ca}(\text{NO}_3)_2$ is dissociated into Ca^{2+} and NO_3^- ions in the solution. When the electrolyte is electrolyzed by a DC voltage, the influent electrons accelerate the dissociation of $\text{CH}_3(\text{CH}_2)_{16}\text{COOH}$ and cause the reduction of H^+ . A large number of $\text{CH}_3(\text{CH}_2)_{16}\text{COO}^-$ ions and hydrogen bubbles form (Eq.(1) and Eq.(2)). Subsequently, the dissociative Ca^{2+} ions capture $\text{CH}_3(\text{CH}_2)_{16}\text{COO}^-$ ions in the absence of H^+ and they deposit in the form of $\text{Ca}[\text{CH}_3(\text{CH}_2)_{16}\text{COO}]_2$ on the surface of the cathode (Eq.(3)).



Calcium stearate deposits on the surface of the pre-treated substrates according to Eq. (3). With electrolysis proceeding, more and more calcium stearate forms on the surface of the pre-treated substrates.

Nitrate ion is electrochemically reducible. Xu et al. [51] prepared superhydrophobic nickel stearate/nickel hydroxide coating on aluminum alloy in an ethanolic stearic acid solution containing nickel nitrate hexahydrate under a DC voltage. They reported that nitrate ion was reduced to ammonium ion but did not give a proof for the existence of ammonium ion. Yoshida et al. [52] reported electrodeposition of crystalline ZnO thin films from zinc nitrate aqueous

solution and nitrate ion was reduced to nitrite ion during the deposition process. In these studies, electroreduction of nitrate ion to either ammonium ion or nitrite ion generated hydroxide ions at the cathode during the deposition process. They considered that the precipitation of coating was triggered by the electrochemical reduction of the nitrate species and the growth mechanism was based on the increase of pH at the working electrode.

In the recent studies, we used the same electrodeposition method as described in this paper to obtain the calcium stearate hydrophobic coating on the anodized magnesium alloy. The only difference was that calcium nitrate was replaced by calcium chloride in the electrolyte solution. This suggests that the electrodeposition of calcium stearate does not depend on the reduction of the nitrate species, which needs further research.

Fig. 4 displays the XRD patterns of the full coating systems. The diffraction patterns of Mg and MgO are from the pre-treated substrates. Apart from this, only the patterns of calcium stearate are observed, indicating that calcium stearate is the main phase composition of the hydrophobic coating. Table 5 shows the elemental composition of the full coating systems determined by EDS. The contents of carbon, oxygen, and calcium are similar for all specimens. This suggests that different surface pre-treatments do not affect the phase compositions of the coatings.

The surface morphologies of the hydrophobic coatings are shown in Fig. 5. All samples are covered with micro-scale protrusions which are composed of nanostructures. However, it is obvious that the diameters of the micro-scale protrusions on the surface of the three samples are different. For the EPEO-HC sample, the protrusions show the largest average size (36 μm , Fig. 5a), followed by the AT-HC (26 μm , Fig. 5b) and the HT-HC (22 μm , Fig. 5c), indicating that the nucleation conditions of the coatings on different pre-treated surfaces are different.

The cross-sectional images of the **full coating systems** are displayed in Fig. 6. The average thickness of the **EPEO** layer is about 8 μm (Fig. 6a) while the average thicknesses of the **AT** layer and the **HT** layer are about 3 μm (Fig. 6b) and 1 μm (Fig. 6c), respectively. The hydrophobic coating grown on the surface of the **EPEO** substrate is thinner compared to other two pre-treatments. Its average thickness is around 17 μm while the thicknesses of the coatings on the surfaces of the **AT** and **HT** substrates are around 27 μm and 22 μm , respectively. Moreover, some irregular pores appear in the hydrophobic coatings of the **AT-HC** and **HT-HC** samples (Fig. 6b and c). Such defects might be disadvantageous for the corrosion resistance of the **AT-HC** and **HT-HC** samples. In contrast, the hydrophobic coating of the **EPEO-HC** specimen is free of larger defects.

3.3 Surface wettability

The wettability of **the pre-treated substrates and full coating systems** was characterized by static water contact angle measurements. Fig. 7 shows the average values of the water contact angles determined on the surfaces of the various specimens. The error bars for each plot indicate maximum and minimum water contact angles on the same specimen. The water contact angle on the surfaces of the pre-treated substrates is 70.3 $^\circ$, 44.2 $^\circ$ and 87.0 $^\circ$ for the **EPEO**, **AT** and **HT**, respectively. **Looking at the full coating systems**, the water contact angle of the **EPEO-HC** is the lowest (118.5 $^\circ$), followed by the **AT-HC** (137.8 $^\circ$) and **HT-HC** (141.5 $^\circ$). The results are consistent with the surface morphologies shown in Fig. 5. The finer the protrusions and the more uniform their sizes are, the higher the water contact angle is. It is obvious that the surface wettability changes from hydrophilicity to hydrophobicity due to the calcium stearate coating formed on the pre-treated substrates.

3.4 Corrosion behavior

The potentiodynamic polarization curves of **the pre-treated substrates and full coating systems** are presented in Fig. 8. The bare magnesium alloy is also tested as a reference. Compared to the bare magnesium alloy, all surface modifications improve the corrosion resistance. The corrosion potential (E_{corr}), corrosion current density (i_{corr}) and breakdown potential (E_{bd}) derived from the potentiodynamic polarization plots are summarized in Table 6. It can be observed that the E_{corr} values of the **full coating systems** are higher than those of the pre-treated ones and in the anodic regions a passivation range exists. The cathodic and anodic current densities at the same polarization are significantly lower, compared to those obtained for the pre-treated ones and the bare magnesium alloy. This clearly indicates that the corrosion resistance of the **full coating system** is much higher than that of the just pre-treated ones thanks to the presence of the hydrophobic coatings. Comparing the polarization curves of the **full coating systems**, it can be stated that the shape of the curves is similar, but the breakdown potential and corrosion resistance are different. The **EPEO-HC** sample shows the best performance and the **HT-HC** is the worst.

The corrosion performance of all the systems was studied by EIS at open circuit potential (OCP). The measurements were performed by immersing these specimens into SBF at 37 ± 0.5 °C. The OCPs of **the pre-treated substrates and full coating systems** are shown in Fig. 9. The trend of the OCP- t curves for different pre-treated substrates is the same (Fig. 9a). The electrode potentials increase rapidly to about -1.70 V (vs. SCE) in a very short time. Then OCPs increase slowly, reaching finally a relative constant value of around -1.61 ± 0.02 V (vs. SCE) after 24 h of immersion. The OCPs of the **full coating systems** increase sharply to more positive values of -1.58 V (vs. SCE) during the first 1 h and show fluctuations around this constant value for the remaining testing time.

Fig. 10 shows the Bode plots of the bare magnesium alloy after immersion in SBF at 37 ± 0.5 °C for 5 min. The values of impedance modulus are very low (around $95 \Omega \cdot \text{cm}^2$ at 0.01 Hz) in this case, indicating that the bare magnesium alloy has a poor corrosion resistance in the SBF solution. The electrochemical impedance spectra of the pre-treated substrates and full coating systems, immersed into the SBF for different times, are depicted in Fig. 11. The symbols are the experimental data and the solid lines are fitting data. Two well defined time constants are observed from the Bode plots for all the pre-treated substrates (Fig. 11a, b and c). The time constant at middle frequency (around 10^2 - 10^3 Hz) is related to the response from the pre-treatment layer and the relaxation process at low frequency (1 Hz) can be ascribed to the electrochemical process at the metal surface. For the full coating systems, EIS data during the first 4 h of immersion can be obtained only within a narrow frequency range (see Fig. 11d, e and f) because of high data scattering at low frequencies. Our previous study suggests that such an effect is caused by an entrapped air layer present at the surfaces of the hydrophobic coatings [48].

For the EPEO (Fig. 11a), the impedance modulus shows a relatively high value for the whole frequency range at 5 min of immersion. It indicates the higher barrier properties of the EPEO layer. However, it drops quickly after 1 h, indicating that water and aggressive ions start to penetrate into the EPEO layer. Afterwards, the modulus increases slightly because of the formation of corrosion products on and in the EPEO layer. The AT (Fig. 11b) shows a low value ($149 \Omega \cdot \text{cm}^2$) of the impedance modulus at 5 min. Subsequently, it increases gradually with the increase of immersion time, suggesting that the AT layer is corroded continuously during immersion in SBF. The impedance modulus of the HT (Fig. 11c) shows a slight increase after 48 h of immersion.

For the EPEO-HC, the impedance modulus reaches $10^5 \Omega \cdot \text{cm}^2$ at around 60 Hz after 5 min of immersion (Fig. 11d). The initial corrosion process is hindered by the hydrophobic coating.

After 1 h the impedance modulus of the specimen decreases dramatically in the full frequency range indicating that the SBF has penetrated into the coating. Afterwards, the modulus gradually increases due to the formation of the corrosion products. Two time constants are visible at high and medium frequencies for the **EPEO-HC** at 5 min, the time constant at high frequency is due to the hydrophobic coating and the other one at the medium frequency is related to the response of the pre-treatment layer.

The modulus of the **AT-HC** shows a continuous decrease during the whole immersion period (Fig. 11e). In contrast, the modulus of the **HT-HC** drops significantly from 5 min to 12 h. After that, it increases slightly until 72 h (Fig. 11f). For the **AT-HC** and **HT-HC** within 4 h of immersion, there are also two time constants at the high frequency and medium frequency region, respectively. The time constant at high frequency is due to the hydrophobic coating and the other one at the medium frequency is related to the response of the pre-treatment layer. After longer immersion (1 h for the **EPEO-HC** and 12 h for the **AT-HC** and the **HT-HC**) the high frequency time constant associated with the hydrophobic coating nearly disappears while another relaxation process appears at low frequency. This new time constant at about 1 Hz can be ascribed to the electrochemical processes at the magnesium alloy/SBF interface.

The equivalent circuit model used to fit the EIS of the pre-treated **substrates** is shown in Fig. 12. In this work, constant phase angle element (Q) is employed to simulate the capacitance behavior, because the pure capacitance cannot give a perfect fitting result in some cases. In this circuit, R_s is the solution resistance, Q_{pr} and R_{pr} represent the capacitance and resistance of the pre-treated layer, Q_{dl} stands for the electrochemical double layer capacitance, and R_{ct} is the charge transfer resistance. Pseudo-inductive behavior can be observed in the case of the pre-treated substrates at low frequency. This kind of response can be caused by low stability of the fast evolving system and triggering of localized corrosion attack.

The equivalent circuit model in Fig. 13a was used to fit the EIS data obtained at 5 min of immersion for the **EPEO-HC** and within first 4 h for the **AT-HC** and **HT-HC**. The equivalent circuit model in Fig. 13b was used to fit the EIS data obtained for the remaining times after the response of the hydrophobic coating is nearly undetectable. In these circuits, Q_{coat} and R_{coat} represent the capacitance and resistance of the hydrophobic coating, Q_{dl} stands for the electrochemical double layer capacitance, and R_{ct} is the charge transfer resistance.

The resistance values obtained from EIS fitting results of **the pre-treated substrates and full coating systems** are presented in Fig. 14. For the pre-treated substrates, the **EPEO** shows the highest R_{pr} value (Fig. 14a) during the whole immersion process. This indicates that the **EPEO** pre-treatment can provide better corrosion protection for the magnesium alloy than the others. After 72 h of immersion, the R_{ct} values (Fig. 14b) for all the pre-treated substrates reach almost the same value (around $250 \Omega \cdot \text{cm}^2$).

The R_{pr} values (Fig. 14c) show the contributions of the pre-treated layers to the overall corrosion resistance of the **full coating systems**. The R_{pr} value of the **EPEO-HC** undergoes a sharp drop at the beginning, which is related to the penetration of the SBF through the coating pores. This is due to the thinnest hydrophobic coating and the lowest water contact angle on the sample surface. Afterwards, the R_{pr} value increases significantly from 1 h to 12 h and a slight increase is also observed from 12 h to 72 h. This might be due to the conversion of the pre-treatment layer. When the **EPEO** layer is **in contact with** the SBF, the hydration of MgO can take place according to the following reactions:



The newly formed $\text{Mg}(\text{OH})_2$ can block the defects and contribute to the overall corrosion resistance [53]. Thus, the R_{pr} value presents an increasing trend.

With the presence of the hydrophobic coating, the **AT-HC** exhibits the highest R_{pr} value (Fig. 14c) within 4 h, because the sample has the thickest coating and better hydrophobicity. This makes it more difficult for the SBF to penetrate the coating and reach the substrate. Afterwards, the R_{pr} value of the **AT-HC** quickly decreases up to 12 h immersion, which might be caused by the penetration of the electrolyte through the hydrophobic coating. After maintaining a certain transient stability, the R_{pr} value represents an obvious drop from 24 h to 48 h, indicating the failure of the hydrophobic coating. After that the R_{pr} value shows a slight increase, which is also caused by newly formed $Mg(OH)_2$ due to the hydrolyzing of MgO .

Compared to the **AT-HC**, the R_{pr} value (Fig. 14c) of the **HT-HC** shows a sharper decrease within the first 12 h, owing to the thinner hydrophobic coating on the surface of the **HT-HC**. As the immersion time increases, the R_{pr} value increases at first and subsequently decreases. These changes of R_{pr} are related to the tradeoff between the sealing of small pores as a result of conversion processes and the formation of new defects and partial failure of the hydrothermal layer.

After SBF penetrates through the **full coating system** and reaches the surface of the Mg alloy, the corrosion processes on the alloy surface start. The R_{ct} values of the **EPEO-HC** and **HT-HC** increase continuously from 12 h to 72 h (Fig. 14d), because the formation of the corrosion products restrains the dissolution of the magnesium alloy. The R_{ct} value for the **AT-HC** shows a slight fluctuation around the initial value.

Though the pre-treatment layers can be degrading during the immersion in SBF (Fig. 11), with the presence of the hydrophobic coating, the R_{pr} values are higher within the immersion time period (Fig. 14a and c). It is also evident that the R_{ct} values of the **full coating systems** (Fig. 14 d) are by far greater than those of the pre-treated substrates alone (Fig. 14 b).

Fig. 15 shows the polarization curves of the **full coating systems** in SBF after 72 h of immersion. The electrochemical parameters are presented in Table 7. A passivation region is observed in the anodic regions of the specimens. The shape and location of the polarization curves for the **AT-HC** and **HT-HC** are very similar, which suggests that the corrosion behavior of the **two samples** is similar after 72 h of immersion. The i_{corr} value of the **EPEO-HC** is 5.65×10^{-8} A/cm², which is about two orders of magnitude lower compared to the **AT-HC** (3.88×10^{-6} A/cm²) and **HT-HC** (3.16×10^{-6} A/cm²). This indicates that the **EPEO-HC** shows the best corrosion resistance after immersion for 72 h, which is consistent with the EIS results.

4. Discussion

The hydrophobicity of the coating surface enhances the initial corrosion resistance of the coated samples (Fig. 11d, e and f) because the surfaces are only partially wetted by the SBF. **This** is related to the high water contact angles and the presence of the entrapped air at the coating/electrolyte interface as previously reported [54-56]. However, the SBF penetrates into the coating as soon as the entrapped air is removed during immersion. Thus, it is important to use an appropriate pre-treatment on the surface of the magnesium alloy prior to the application of the hydrophobic coating in order to stabilize the magnesium alloy/calcium stearate coating interface. The obtained results suggest that the pre-treatment influences also the coating morphology, the coating thickness and the adhesion between the hydrophobic coating and the substrate. The hydrophobicity of the coating surface is obviously influenced by the surface morphology **of the coating**.

However, using a pre-treatment with too high barrier properties, such as an original PEO coating, can prohibit the electrodeposition of the hydrophobic coating. Therefore a partial dissolution of the PEO layer during the etching in phosphoric acid can help to reduce the IR drop across the PEO layer and allow the electrodeposition process.

For the **EPEO-HC**, the thickness of the hydrophobic coating is the thinnest (Fig. 6a) and the water contact angle is the lowest (Fig. 7). In this case, the corrosion resistance of the sample should be the lowest. However, the **EPEO-HC** exhibits the best corrosion protection properties (Fig. 8) and the highest R_{pr} value between 12 h and 72 h of immersion (Fig. 14c). This can be attributed to the presence of the thickest pre-treatment layer at the Mg alloy surface (Fig. 6a), which provides further protection for the alloy. Once the coating is penetrated, the **EPEO** layer will be exposed to the SBF and **hydration of MgO** can take place. The formed $Mg(OH)_2$ can block the defects existing in the EPEO layer and thus contribute additionally to the corrosion resistance. **Furthermore**, it is not easy for the SBF to reach the magnesium alloy surface because the **EPEO** layer is thick and compact enough to resist the corrosion attack. Therefore, the **EPEO-HC** exhibits the best corrosion resistance.

The **AT-HC** has the thickest coating and better hydrophobicity, which provides the best corrosion protection properties for the **full coating system** at the initial stage of the immersion. The coating can still remain protective long after the SBF has started to penetrate into the coating. This is illustrated by the relatively higher R_{pr} and R_{ct} values between 12 h and 24 h (Fig. 14c and d).

For the **HT-HC**, the combination of the highest hydrophobicity and a relative thick coating results in the highest R_{pr} value at the initial stage of the immersion process (Fig. 14c). However, the hydrothermal layer is very thin and when water and aggressive ions pass through the hydrophobic coating, the hydrothermal layer does not provide much protection and degradation of the **full coating system** is fast. The **overall** corrosion resistance of the **HT-HC** is the lowest.

The results clearly indicate that the pre-treatment prior to the hydrophobic coating is very important for the long term corrosion resistance of the **full coating system**.

5. Conclusions

The effect of pre-treatment on the electrodeposition of calcium stearate based hydrophobic coating and consequently on the corrosion protection properties has been investigated and discussed. The following conclusions can be drawn:

1. The hydrophobic coating cannot be directly deposited on the PEO substrate because of high barrier properties of the PEO layer. However, it can be easily obtained on the **EPEO**, **AT**, and **HT** substrates.
2. The pre-treatment of the magnesium alloy prior to the hydrophobic coating application has a strong influence **on** the formation of the coating. The pre-treatment affects the thickness and surface morphology of the hydrophobic coating but does not alter the phase composition of the coating. The surface wettability **of the hydrophobic coating** is also affected since it strongly depends on the surface morphology.
3. The pre-treatment layer plays an important role in the corrosion resistance of the **full coating system** especially after the electrolyte has penetrated the hydrophobic coating. The EPEO pre-treatment owns a compact inner layer and the thickest pre-treatment layer on the AZ21 Mg alloy. It ensures the highest stability at coating/EPEO and EPEO/metal interfaces leading to superior corrosion resistance of the **EPEO-HC**.

Acknowledgements

The authors thank Mr. Ulrich Burmester and Mr. Gert Wiese for the technical support during the course of this work. Yufen Zhang thanks China Scholarship Council for the award of fellowship and funding. The Project was supported by the National Natural Science Foundation of China (Grant No. 51272055 and 51501050).

References

- [1] W. Ximei, Z. Liqun, L. Huicong, L. Weiping, Influence of surface pretreatment on the anodizing film of Mg alloy and the mechanism of the ultrasound during the pretreatment, *Surface and Coatings Technology*, 202 (2008) 4210-4217.
- [2] G. Wu, J.M. Ibrahim, P.K. Chu, Surface design of biodegradable magnesium alloys — A review, *Surface and Coatings Technology*, 233 (2013) 2-12.
- [3] N.T. Kirkland, N. Birbilis, M.P. Staiger, Assessing the corrosion of biodegradable magnesium implants: a critical review of current methodologies and their limitations, *Acta biomaterialia*, 8 (2012) 925-936.
- [4] H. Hornberger, S. Virtanen, A.R. Boccaccini, Biomedical coatings on magnesium alloys - a review, *Acta biomaterialia*, 8 (2012) 2442-2455.
- [5] N. Li, Y. Zheng, Novel Magnesium Alloys Developed for Biomedical Application: A Review, *Journal of Materials Science & Technology*, 29 (2013) 489-502.
- [6] Y. Chen, Z. Xu, C. Smith, J. Sankar, Recent advances on the development of magnesium alloys for biodegradable implants, *Acta biomaterialia*, 10 (2014) 4561-4573.
- [7] I.S. Bayer, A. Steele, P.J. Martorana, E. Loth, L. Miller, Superhydrophobic cellulose-based bionanocomposite films from Pickering emulsions, *Applied Physics Letters*, 94 (2009) 163902.
- [8] F. Witte, The history of biodegradable magnesium implants: a review, *Acta biomaterialia*, 6 (2010) 1680-1692.
- [9] M.P. Staiger, A.M. Pietak, J. Huadmai, G. Dias, Magnesium and its alloys as orthopedic biomaterials: a review, *Biomaterials*, 27 (2006) 1728-1734.
- [10] N.T. Kirkland, Magnesium biomaterials: past, present and future, *Corrosion Engineering, Science and Technology*, 47 (2012) 322-328.
- [11] Y. Xin, T. Hu, P.K. Chu, In vitro studies of biomedical magnesium alloys in a simulated physiological environment: a review, *Acta biomaterialia*, 7 (2011) 1452-1459.

- [12] B. Liu, X. Zhang, G.Y. Xiao, Y.P. Lu, Phosphate chemical conversion coatings on metallic substrates for biomedical application: a review, *Materials science & engineering. C, Materials for biological applications*, 47 (2015) 97-104.
- [13] P. Amaravathy, S. Sowndarya, S. Sathyanarayanan, N. Rajendran, Novel sol gel coating of Nb₂O₅ on magnesium alloy for biomedical applications, *Surface and Coatings Technology*, 244 (2014) 131-141.
- [14] Y. Gao, A. Yerokhin, A. Matthews, Deposition and evaluation of duplex hydroxyapatite and plasma electrolytic oxidation coatings on magnesium, *Surface and Coatings Technology*, 269 (2015) 170-182.
- [15] H. Hoche, S. Groß, M. Oechsner, Development of new PVD coatings for magnesium alloys with improved corrosion properties, *Surface and Coatings Technology*, 259 (2014) 102-108.
- [16] X. Yang, M. Li, X. Lin, L. Tan, G. Lan, L. Li, Q. Yin, H. Xia, Y. Zhang, K. Yang, Enhanced in vitro biocompatibility/bioactivity of biodegradable Mg–Zn–Zr alloy by micro-arc oxidation coating contained Mg₂SiO₄, *Surface and Coatings Technology*, 233 (2013) 65-73.
- [17] P. Salunke, V. Shanov, F. Witte, High purity biodegradable magnesium coating for implant application, *Materials Science and Engineering: B*, 176 (2011) 1711-1717.
- [18] A. Saijo, K. Murakami, M. Hino, T. Kanadani, Effect of Environmentally Friendly Anodization on the Mechanical Properties and Microstructure of AZ91D Magnesium Alloy, *Materials Transactions*, 49 (2008) 903-908.
- [19] N.V. Murillo-Gutiérrez, F. Ansart, J.P. Bonino, M.J. Menu, M. Gressier, Protection against corrosion of magnesium alloys with both conversion layer and sol–gel coating, *Surface and Coatings Technology*, 232 (2013) 606-615.
- [20] Z. Xie, G. Yu, T. Li, Z. Wu, B. Hu, Dynamic behavior of electroless nickel plating reaction on magnesium alloys, *Journal of Coatings Technology and Research*, 9 (2011) 107-114.

- [21] M. Mohedano, C. Blawert, M.L. Zheludkevich, Cerium-based sealing of PEO coated AM50 magnesium alloy, *Surface and Coatings Technology*, 269 (2015) 145-154.
- [22] A. Zomorodian, C. Santos, M.J. Carmezim, T.M.e. Silva, J.C.S. Fernandes, M.F. Montemor, “In-vitro” corrosion behaviour of the magnesium alloy with Al and Zn (AZ31) protected with a biodegradable polycaprolactone coating loaded with hydroxyapatite and cephalexin, *Electrochimica Acta*, 179 (2015) 431-440.
- [23] Z. She, Q. Li, Z. Wang, L. Li, F. Chen, J. Zhou, Novel method for controllable fabrication of a superhydrophobic CuO surface on AZ91D magnesium alloy, *ACS applied materials & interfaces*, 4 (2012) 4348-4356.
- [24] W. Xu, J. Song, J. Sun, Y. Lu, Z. Yu, Rapid fabrication of large-area, corrosion-resistant superhydrophobic Mg alloy surfaces, *ACS applied materials & interfaces*, 3 (2011) 4404-4414.
- [25] D. Zang, R. Zhu, C. Wu, X. Yu, Y. Zhang, Fabrication of stable superhydrophobic surface with improved anticorrosion property on magnesium alloy, *Scripta Materialia*, 69 (2013) 614-617.
- [26] T. Ishizaki, Y. Masuda, M. Sakamoto, Corrosion resistance and durability of superhydrophobic surface formed on magnesium alloy coated with nanostructured cerium oxide film and fluoroalkylsilane molecules in corrosive NaCl aqueous solution, *Langmuir : the ACS journal of surfaces and colloids*, 27 (2011) 4780-4788.
- [27] Y. Huang, D.K. Sarkar, X.G. Chen, A one-step process to engineer superhydrophobic copper surfaces, *Materials Letters*, 64 (2010) 2722-2724.
- [28] Z. Kang, X. Lai, J. Sang, Y. Li, Fabrication of hydrophobic/super-hydrophobic nanofilms on magnesium alloys by polymer plating, *Thin Solid Films*, 520 (2011) 800-806.

- [29] Y. Liu, X. Yin, J. Zhang, Y. Wang, Z. Han, L. Ren, Biomimetic hydrophobic surface fabricated by chemical etching method from hierarchically structured magnesium alloy substrate, *Applied Surface Science*, 280 (2013) 845-849.
- [30] Z. Wang, Y. Su, Q. Li, Y. Liu, Z. She, F. Chen, L. Li, X. Zhang, P. Zhang, Researching a highly anti-corrosion superhydrophobic film fabricated on AZ91D magnesium alloy and its anti-bacteria adhesion effect, *Materials Characterization*, 99 (2015) 200-209.
- [31] P. Wan, J. Wu, L. Tan, B. Zhang, K. Yang, Research on super-hydrophobic surface of biodegradable magnesium alloys used for vascular stents, *Materials science & engineering. C, Materials for biological applications*, 33 (2013) 2885-2890.
- [32] X.-j. Cui, X.-z. Lin, C.-h. Liu, R.-s. Yang, X.-w. Zheng, M. Gong, Fabrication and corrosion resistance of a hydrophobic micro-arc oxidation coating on AZ31 Mg alloy, *Corrosion Science*, 90 (2015) 402-412.
- [33] J. Wang, D. Li, Q. Liu, X. Yin, Y. Zhang, X. Jing, M. Zhang, Fabrication of hydrophobic surface with hierarchical structure on Mg alloy and its corrosion resistance, *Electrochimica Acta*, 55 (2010) 6897-6906.
- [34] M. Liang, Y. Wei, L. Hou, H. Wang, Y. Li, C. Guo, Fabrication of a super-hydrophobic surface on a magnesium alloy by a simple method, *Journal of Alloys and Compounds*, 656 (2016) 311-317.
- [35] N. Wang, J. Xi, S. Wang, H. Liu, L. Feng, L. Jiang, Long-term and thermally stable superhydrophobic surfaces of carbon nanofibers, *Journal of colloid and interface science*, 320 (2008) 365-368.
- [36] Z. Chen, L. Hao, A. Chen, Q. Song, C. Chen, A rapid one-step process for fabrication of superhydrophobic surface by electrodeposition method, *Electrochimica Acta*, 59 (2012) 168-171.

- [37] Z. Chen, L. Hao, C. Chen, A fast electrodeposition method for fabrication of lanthanum superhydrophobic surface with hierarchical micro-nanostructures, *Colloids and Surfaces A: Physicochemical and Engineering Aspects*, 401 (2012) 1-7.
- [38] Z. Chen, F. Li, L. Hao, A. Chen, Y. Kong, One-step electrodeposition process to fabricate cathodic superhydrophobic surface, *Applied Surface Science*, 258 (2011) 1395-1398.
- [39] T. Kamegawa, Y. Shimizu, H. Yamashita, Superhydrophobic surfaces with photocatalytic self-cleaning properties by nanocomposite coating of TiO₂ and polytetrafluoroethylene, *Adv Mater*, 24 (2012) 3697-3700.
- [40] D. Zang, R. Zhu, W. Zhang, J. Wu, X. Yu, Y. Zhang, Stearic acid modified aluminum surfaces with controlled wetting properties and corrosion resistance, *Corrosion Science*, 83 (2014) 86-93.
- [41] W. Li, Z. Kang, Fabrication of corrosion resistant superhydrophobic surface with self-cleaning property on magnesium alloy and its mechanical stability, *Surface and Coatings Technology*, 253 (2014) 205-213.
- [42] H. Ogihara, T. Katayama, T. Saji, One-step electrophoretic deposition for the preparation of superhydrophobic silica particle/trimethylsiloxysilicate composite coatings, *Journal of colloid and interface science*, 362 (2011) 560-566.
- [43] P. Wang, D. Zhang, R. Qiu, J. Wu, Y. Wan, Super-hydrophobic film prepared on zinc and its effect on corrosion in simulated marine atmosphere, *Corrosion Science*, 69 (2013) 23-30.
- [44] P. Wang, D. Zhang, R. Qiu, J. Wu, Super-hydrophobic metal-complex film fabricated electrochemically on copper as a barrier to corrosive medium, *Corrosion Science*, 83 (2014) 317-326.

- [45] P. Wang, D. Zhang, R. Qiu, Y. Wan, J. Wu, Green approach to fabrication of a super-hydrophobic film on copper and the consequent corrosion resistance, *Corrosion Science*, 80 (2014) 366-373.
- [46] P. Wang, D. Zhang, R. Qiu, B. Hou, Super-hydrophobic film prepared on zinc as corrosion barrier, *Corrosion Science*, 53 (2011) 2080-2086.
- [47] T. Ishizaki, M. Sakamoto, Facile formation of biomimetic color-tuned superhydrophobic magnesium alloy with corrosion resistance, *Langmuir : the ACS journal of surfaces and colloids*, 27 (2011) 2375-2381.
- [48] Y. Zhang, S. Tang, J. Hu, T. Lin, Formation mechanism and corrosion resistance of the hydrophobic coating on anodized magnesium, *Corrosion Science*, (2016).
- [49] T. Kokubo, H. Takadama, How useful is SBF in predicting in vivo bone bioactivity?, *Biomaterials*, 27 (2006) 2907-2915.
- [50] W.F. Ng, M.H. Wong, F.T. Cheng, Stearic acid coating on magnesium for enhancing corrosion resistance in Hanks' solution, *Surface and Coatings Technology*, 204 (2010) 1823-1830.
- [51] N. Xu, D.K. Sarkar, X.G. Chen, W.P. Tong, Corrosion performance of superhydrophobic nickel stearate/nickel hydroxide thin films on aluminum alloy by a simple one-step electrodeposition process, *Surface and Coatings Technology*, 302 (2016) 173-184.
- [52] T. Yoshida, M. Tochimoto, D. Schlettwein, D. Wöhrle, T. Sugiura, M. Minoura, Self-assembly of zinc oxide thin films modified with tetrasulfonated metallophthalocyanines by one-step electrodeposition, *Chemistry of Materials*, 11 (1999) 2657-2667.
- [53] J. Liang, P.B. Srinivasan, C. Blawert, W. Dietzel, Influence of chloride ion concentration on the electrochemical corrosion behaviour of plasma electrolytic oxidation coated AM50 magnesium alloy, *Electrochimica Acta*, 55 (2010) 6802-6811.

- [54] T. Ishizaki, J. Hieda, N. Saito, N. Saito, O. Takai, Corrosion resistance and chemical stability of super-hydrophobic film deposited on magnesium alloy AZ31 by microwave plasma-enhanced chemical vapor deposition, *Electrochimica Acta*, 55 (2010) 7094-7101.
- [55] Y. Liu, S. Li, J. Zhang, J. Liu, Z. Han, L. Ren, Corrosion inhibition of biomimetic super-hydrophobic electrodeposition coatings on copper substrate, *Corrosion Science*, 94 (2015) 190-196.
- [56] L. Ejenstam, A. Swerin, J. Pan, P.M. Claesson, Corrosion protection by hydrophobic silica particle-polydimethylsiloxane composite coatings, *Corrosion Science*, 99 (2015) 89-97.

Figure/Table captions

Fig. 1. XRD patterns of the pre-treated substrates: (a) PEO, (b) EPEO, (c) AT and (d) HT.

Fig. 2. SEM images of the pre-treated substrates: (a) PEO, (b) EPEO, (c) AT and (d) HT. The inserts are high magnification images respectively.

Fig. 3. Current density-time curves measured at different pre-treated substrates during the cathodic electrodeposition process in an ethanol mixed solution (0.05 mol/L $\text{Ca}(\text{NO}_3)_2$, 0.05 mol/L stearic acid and the solvent was ethanol). A constant working voltage of 50 V was applied. Wherein, different pre-treated substrates ((a) PEO, (b) EPEO, (c) AT and (d) HT) were used as cathode and a graphite sheet was used as anode.

Fig. 4. XRD patterns of the full coating systems: (a) EPEO-HC, (b) AT-HC and (c) HT-HC.

Fig. 5. SEM images of the full coating systems: (a) EPEO-HC, (b) AT-HC and (c) HT-HC. The inserts are high magnification images respectively.

Fig. 6. Cross-sectional images of the full coating systems: (a) EPEO-HC, (b) AT-HC and (c) HT-HC.

Fig. 7. Static water contact angles measured on the surfaces of the pre-treated substrates (EPEO, AT and HT) and full coating systems (EPEO-HC, AT-HC and HT-HC).

Fig. 8. Potentiodynamic polarization curves of AZ21 Mg alloy, the pre-treated substrates (EPEO, AT and HT) and full coating systems (EPEO-HC, AT-HC and HT-HC) in SBF at 37 ± 0.5 °C.

Fig. 9. OCP-*t* curves of (a) the pre-treated substrates and (b) the full coating systems in SBF at 37 ± 0.5 °C.

Fig. 10. Bode plots of AZ21 Mg alloy after immersion in SBF at 37 ± 0.5 °C for 5 min.

Fig. 11. Bode plots evolution of the pre-treated substrates ((a) EPEO, (b) AT and (c) HT) and full coating systems ((d) EPEO-HC, (e) AT-HC and (f) HT-HC) in SBF at 37 ± 0.5 °C (symbols are experimental data and solid lines are fitting data).

Fig. 12. Equivalent circuit model used for numerical fitting of the pre-treated substrates (EPEO, AT and HT) during the entire SBF immersion process at 37 ± 0.5 °C.

Fig. 13. Equivalent circuit models used for numerical fitting of the full coating systems during the different SBF immersion periods at 37 ± 0.5 °C: (a) 5 min for EPEO-HC, 5 min to 4 h for AT-HC and HT-HC; (b) 1 h to 72 h for EPEO-HC, 12 h to 72 h for AT-HC and HT-HC.

Fig. 14. The evolution of resistance values (obtained from EIS fitting results) with immersion time in SBF at 37 ± 0.5 °C for the pre-treated substrates ((a) R_{pr} and (b) R_{ct}) and full coating systems ((c) R_{pr} and (d) R_{ct}).

Fig. 15. Potentiodynamic polarization curves obtained for the full coating systems after immersion in SBF at 37 ± 0.5 °C for 72 h.

Table 1 Chemical composition of the received material.

Table 2 Details of the pre-treatments on AZ21 Mg alloy.

Table 3 Details of the cathodic electrodeposition of the hydrophobic coating formed on different pre-treated substrates.

Table 4 Surface composition of AZ21 Mg alloy and the pre-treated substrates determined by EDS analysis.

Table 5 Surface composition of the full coating systems determined by EDS analysis.

Table 6 Electrochemical data obtained from potentiodynamic polarization curves of AZ21 Mg alloy, the pre-treated substrates and full coating systems in SBF at 37 ± 0.5 °C.

Table 7 Electrochemical data obtained from potentiodynamic polarization curves of the full coating systems after immersion in SBF at 37 ± 0.5 °C for 72 h.

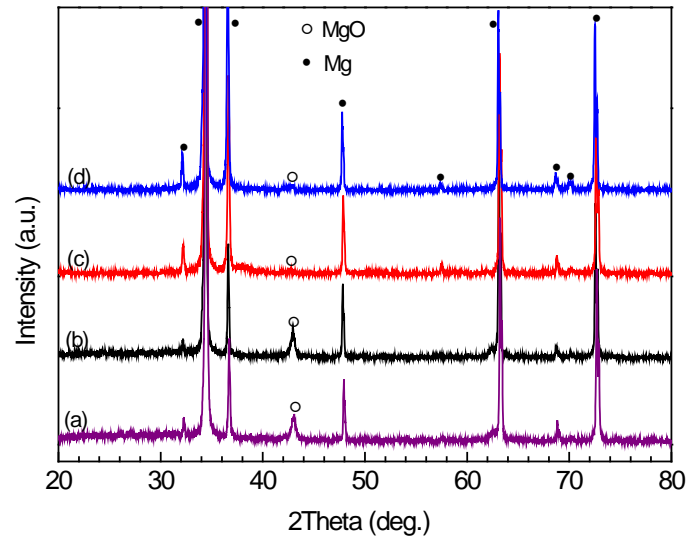


Fig. 1. XRD patterns for differently pre-treated substrates on AZ21 Mg alloy: (a) PEO; (b) EPEO; (c) AT; (d) HT.

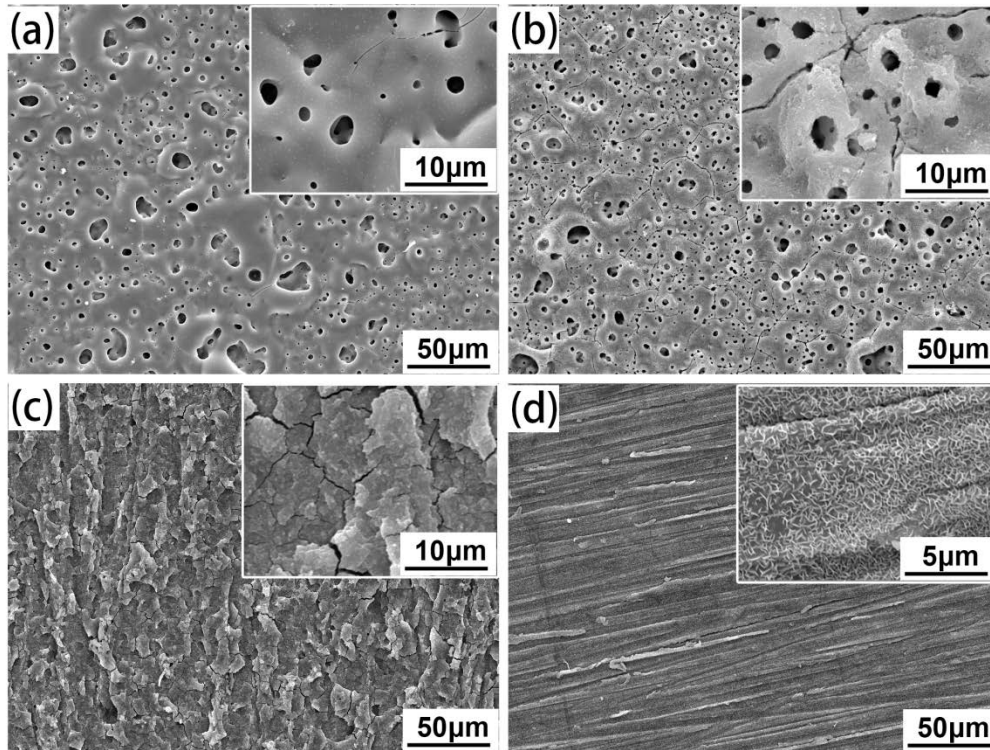


Fig. 2. SEM images for differently pre-treated substrates on AZ21 Mg alloy: (a) PEO; (b) EPEO; (c) AT; (d) HT.

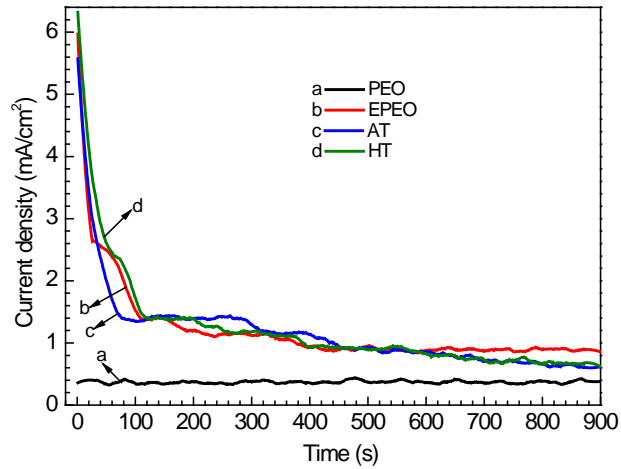


Fig. 3. Current density of differently pre-treated substrates evolved with time during the cathodic electrodeposition process in an ethanol-based electrolyte (0.05 mol/L $(\text{Ca}(\text{NO}_3)_2)$, 0.05 mol/L stearic acid and ethanol) under a constant working voltage of 50 V. Wherein, the pre-treated substrate used as cathode and a graphite sheet used as anode.

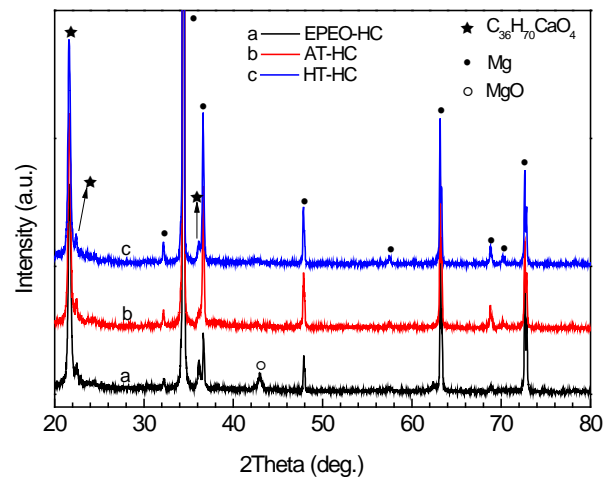


Fig. 4. XRD patterns of the hydrophobic coating covered specimens on differently pre-treated substrates.

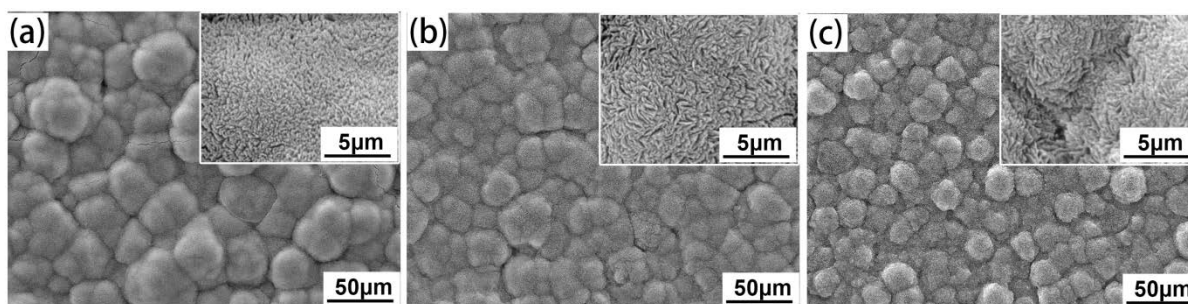


Fig. 5. SEM images of the hydrophobic coating covered specimens on differently pre-treated substrates: (a) EPEO-HC; (b) AT-HC; (c) HT-HC.

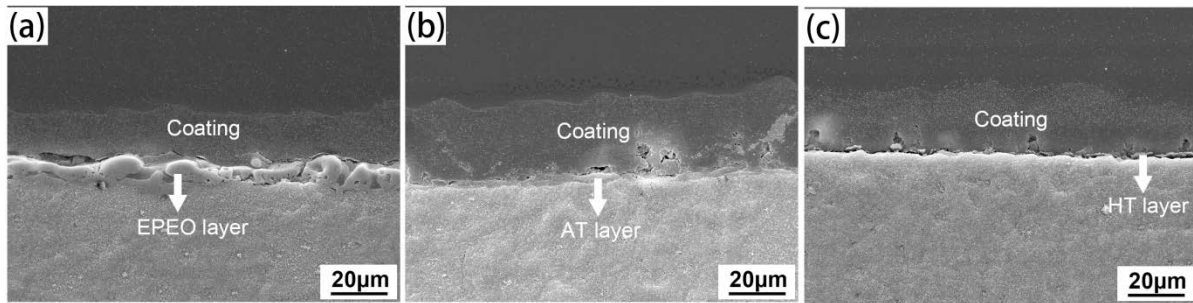


Fig. 6. Cross-sectional images of the hydrophobic coating covered specimens on differently pre-treated substrates: (a) EPEO-HC; (b) AT-HC; (c) HT-HC.

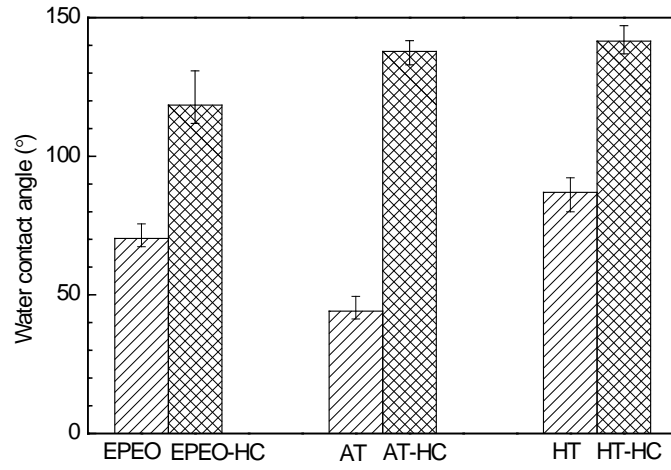


Fig. 7. Static water contact angles on the pre-treated substrates and the hydrophobic coating covered specimens.

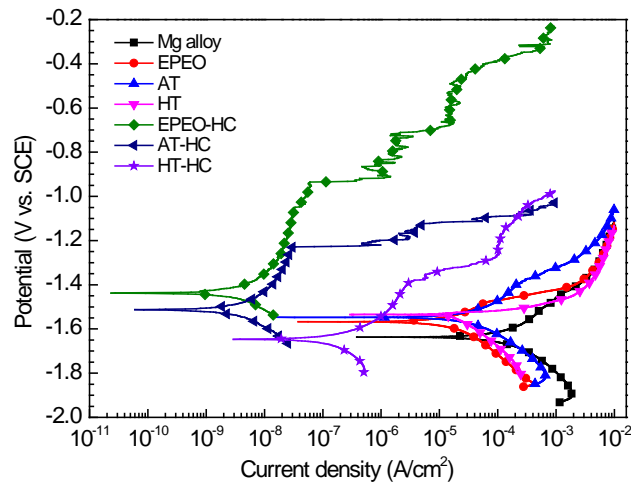


Fig. 8. Polarization curves of Mg alloy, differently pre-treated substrates, and the hydrophobic coating covered specimens in SBF at 37 ± 0.5 °C.

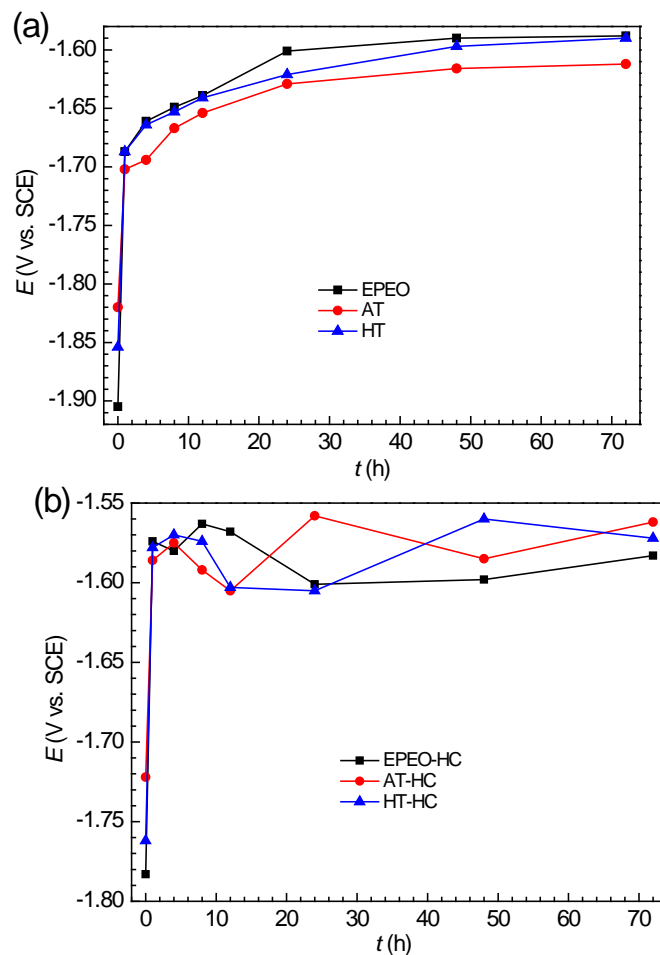


Fig. 9. OCP- t curves of the specimens in SBF at 37 ± 0.5 °C: (a) the pre-treated substrates; (b) the

hydrophobic coating covered specimens.

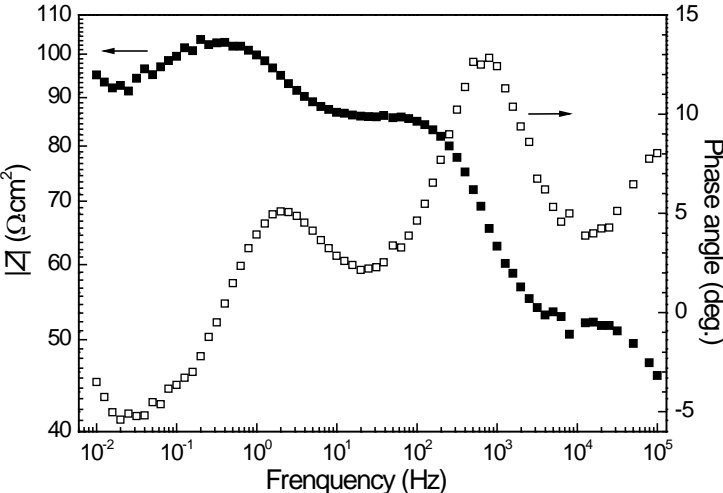


Fig. 10. Bode plots of AZ21 Mg alloy in SBF at 37 ± 0.5 °C after 5 min of immersion.

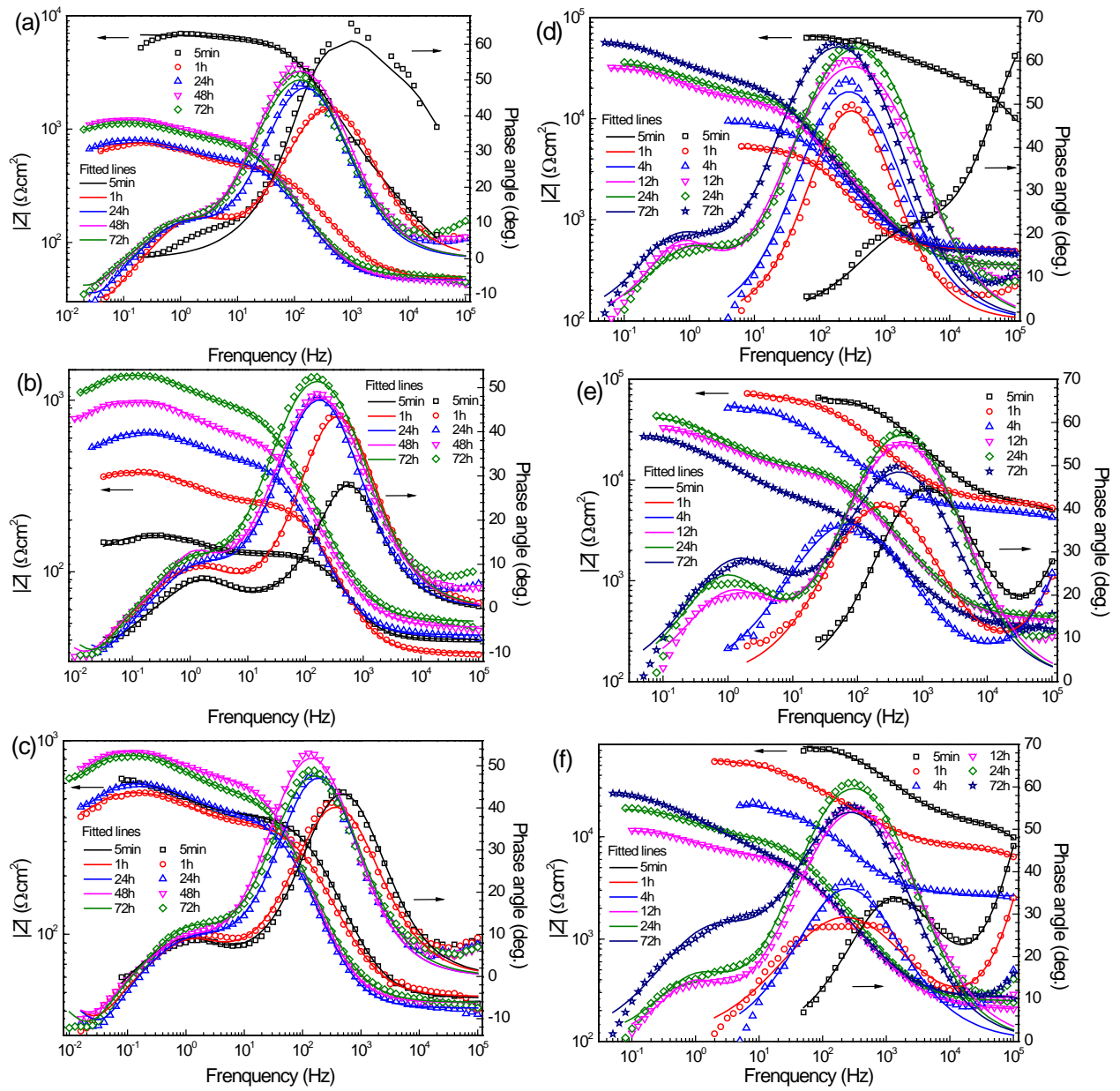


Fig. 11. Bode plots evolution of the pre-treated substrates and the hydrophobic coating covered specimens in SBF at 37 ± 0.5 °C (symbols are experimental data and solid lines are fitting data): (a) EPEO; (b) AT; (c) HT; (d) EPEO-HC; (e) AT-HC; (f) HT-HC.

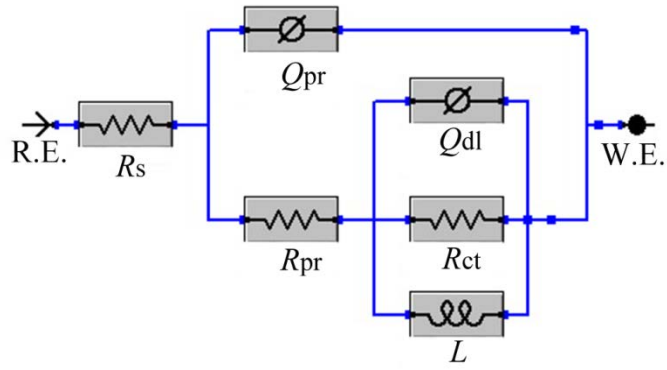


Fig. 12. Equivalent circuit model used for numerical fitting of all the pre-treated substrates during the SBF immersion at 37 ± 0.5 °C.

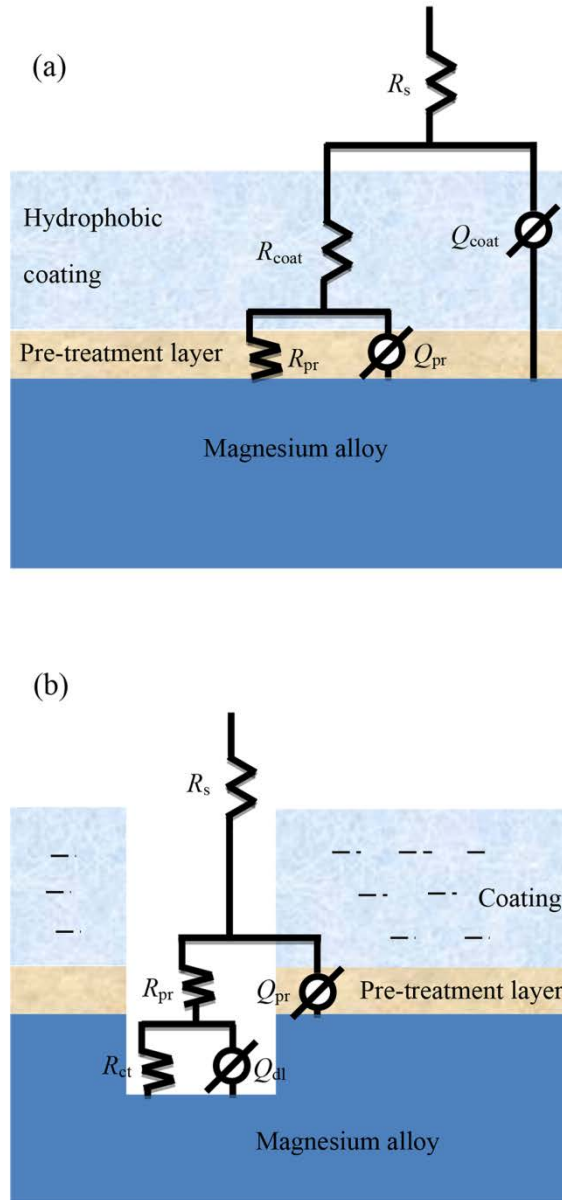


Fig. 13. Equivalent circuit models used for numerical fitting of the hydrophobic coating covered specimens during different SBF immersion periods at 37 ± 0.5 °C: (a) 5 min for EPEO-HC, within 4 h for AT-HC and HT-HC; (b) 1 h–72 h for EPEO-HC, 12 h–72 h for AT-HC and HT-HC.

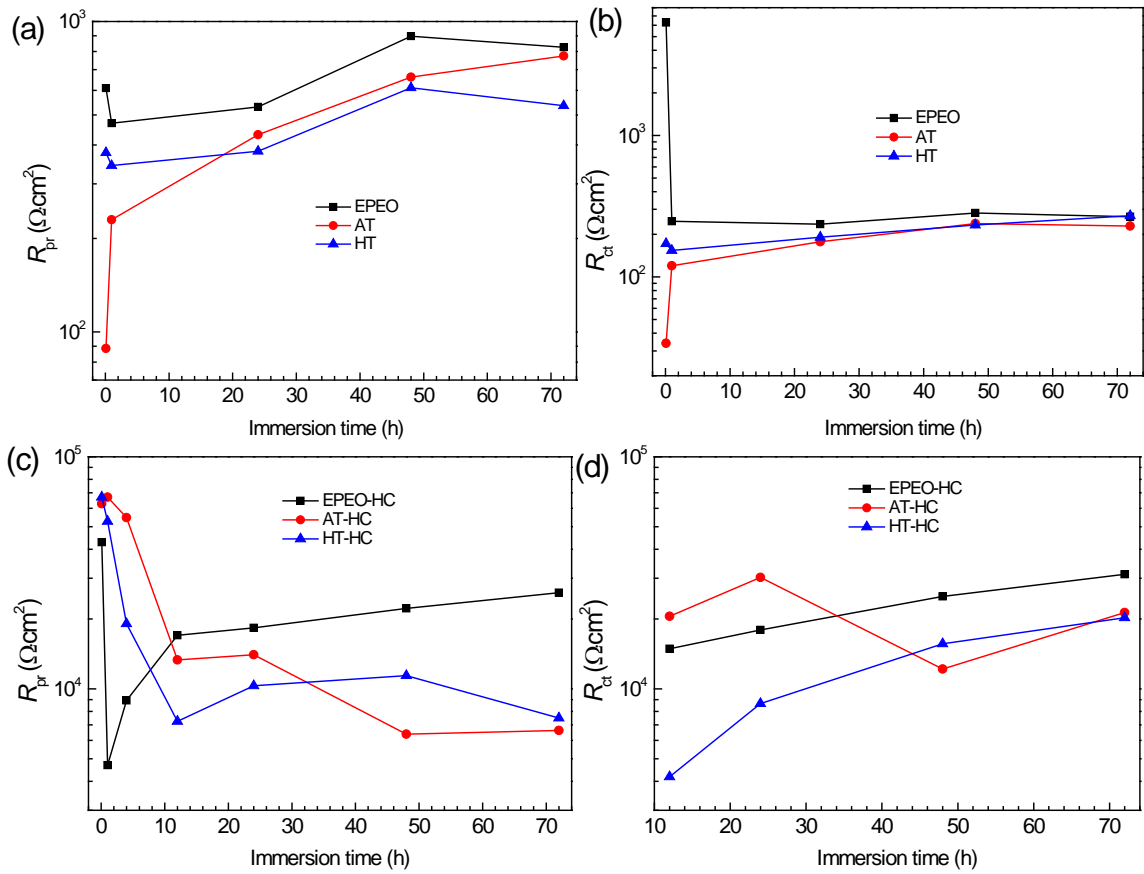


Fig. 14. EIS fitting parameters for the pre-treated substrates: (a) R_{pr} (b) R_{ct} , and for hydrophobic coating covered specimens: (c) R_{pr} (d) R_{ct} .

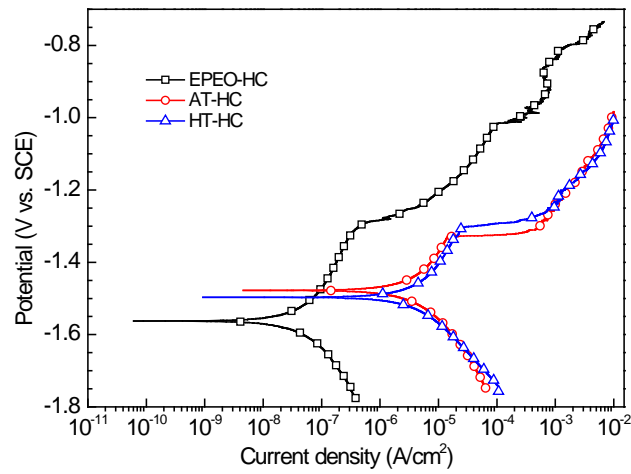


Fig. 15. Polarization curves of the **hydrophobic coating covered specimens** after immersion in SBF at 37 ± 0.5 °C for 72 h.

Table 1 Chemical composition of the received material.

Element	Al	Cu	Mn	Fe	Ni
wt.%	1.92000	0.01330	0.37700	0.01200	0.00108
Element	Zn	Be	Si	Ag	Ca
wt.%	1.18000	0.00004	0.05190	<0.00010	0.00444
Element	Sn	Zr	Ce	La	Mg
wt.%	<0.00050	<0.00060	0.00535	0.01410	96.42000

Table 2 Details of the pre-treatments on AZ21 Mg alloy.

Pre-treatments	Electrolyte	Parameters
Plasma electrolytic oxidation (PEO)	Ca(OH) ₂ 2 g/L Na ₃ PO ₄ 12 g/L	380 V 0.8 A 20 °C 5 min <i>t</i> _{on} = 0.5 ms <i>t</i> _{off} = 4.5ms Cathode: steel
	H ₃ PO ₄ 60 g/L	Room temperature 10 s
Etched plasma electrolytic oxidation (EPEO)		
Anodizing treatment (AT)	Na ₂ C ₂ O ₄ 2.5 g/L NaOH 240 g/L C ₂ H ₆ O ₂ 65 ml/L	Direct current 4 V 40 °C 10 min Cathode: steel
Hydrothermal treatment (HT)		90 °C Humidity 90% 24 h

Table 3 Details of the cathodic electrodeposition of the hydrophobic coating formed on different pre-treated substrates.

Hydrophobic coatings (HC)	Electrolyte	Parameters
Coating deposited on PEO pre-treated substrate (PEO-HC)	Ca(NO ₃) ₂ 0.05 mol/L	Direct current
Coating deposited on EPEO pre-treated substrate (EPEO-HC)	Stearic acid 0.05 mol/L	50 V 60 min
Coating deposited on AT pre-treated substrate (AT-HC)	Solvent: ethanol (≥99.5%)	Room temperature
Coating deposited on HT pre-treated substrate (HT-HC)		Cathode: the pre-treated substrate Anode: a graphite sheet

*If not a specific coating is addressed the combination of pre-treatment and hydrophobic coating is referred to as full coating system.

Table 4 Surface composition of AZ21 Mg alloy and the pre-treated substrates determined by EDS analysis.

Concentration (wt.%)	C	O	Na	Mg	Al	P	Ca	Zn
Mg alloy	-	-	2.0	95.6	1.2	-	-	1.2
PEO	-	38.2	3.8	39.2	0.5	17.7	0.3	0.4
EPEO	-	37.3	2.7	42.6	0.5	16.0	0.2	0.9
AT	5.1	36.4	1.7	55	0.8	-	-	0.9
HT	-	9.4	2.6	85	1.9	-	-	1.1

Table 5 Surface composition of the **full coating systems** determined by EDS analysis.

Concentration (wt.%)	C	O	Ca
EPEO-HC	62.8	20.4	16.7
AT-HC	58.9	21.9	19.1
HT-HC	59.6	21.6	18.8

Table 6 Electrochemical data obtained from potentiodynamic polarization curves of AZ21 Mg alloy, the pre-treated substrates and full coating systems in SBF at 37 ± 0.5 °C.

Specimens	E_{corr} (V vs. SCE)	i_{corr} (A/cm ²)	E_{bd} (V vs. SCE)
Mg alloy	-1.64 ± 0.01	$(2.48 \pm 0.42) \times 10^{-4}$	
EPEO	-1.57 ± 0.02	$(3.01 \pm 1.99) \times 10^{-5}$	
AT	-1.55 ± 0.01	$(3.22 \pm 0.58) \times 10^{-5}$	
HT	-1.53 ± 0.01	$(3.52 \pm 0.33) \times 10^{-5}$	
EPEO-HC	-1.44 ± 0.03	$(3.59 \pm 1.95) \times 10^{-9}$	-0.94 ± 0.03
AT-HC	-1.51 ± 0.02	$(3.10 \pm 4.42) \times 10^{-9}$	-1.23 ± 0.02
HT-HC	-1.65 ± 0.03	$(1.89 \pm 0.96) \times 10^{-7}$	-1.38 ± 0.02

Table 7 Electrochemical data obtained from potentiodynamic polarization curves of the full coating systems after immersion in SBF at 37 ± 0.5 °C for 72 h.

Specimens	E_{corr} (V vs. SCE)	i_{corr} (A/cm ²)	E_{bd} (V vs. SCE)
EPEO-HC	-1.56 ± 0.01	$(5.65 \pm 1.32) \times 10^{-8}$	-1.30 ± 0.02
AT-HC	-1.48 ± 0.02	$(3.88 \pm 2.24) \times 10^{-6}$	-1.33 ± 0.01
HT-HC	-1.50 ± 0.02	$(3.16 \pm 1.21) \times 10^{-6}$	-1.31 ± 0.02